scientific reports

Check for updates

OPEN

Evaluation and synthesis of perovskite crystals as high-Z sensors for hybrid pixel detectors

R. B. Campanelli[1,2]✉, G. S. Gomes[1], M. M. Donatti[1], L. S. Perissinotto[1], A. D. Pereira[1], E. B. Antonio[1], P. L. Vincoletto[1], M. G. Fernandes[1], L. S. Araujo[1], J. M. Polli[1,3] & F. C. Marques[2,3]

High-energy photon imaging experiments are crucial techniques in synchrotron facilities, often employing hybrid pixel detectors for these operations. These detectors combine a photo-sensitive semiconductor component with a pixelated microelectronic Application Specific Integrated Circuit (ASIC) for signal processing and image formation. However, detecting photons above 90 keV poses significant challenges, even for heavy semiconductors, due to lower photoelectric absorption cross-section at this energy range. Nevertheless, lead-based perovskites, such as $CsPbBr_3$, are remarkable alternatives as they present excellent cross-section values and noteworthy transport properties, contributing to increased high-energy detection efficiencies. Here, we employ a chemical synthesis route for $CsPbBr_3$ single-crystals, enabling experimental measurements of carrier mobility of 100.7 cm^2 /Vs. We also developed a simulation algorithm to calculate the current pulses generated on pixelated electrodes. Our simulations evaluate $CsPbBr_3$'s performance coupled with the latest photon-counter ASIC developed by CERN, the Timepix4. Our findings indicate that $CsPbBr_3$ crystals require intense applied electric fields, around 1 kV/mm, for accurate signal integration. Furthermore, we observed no correlation between incident energy and induced pulse width. Through microelectronics simulations, we demonstrate that the signal formation behavior of $CsPbBr_3$ is compatible with Timepix4 ASICs, consequently establishing operational guidelines for employing this promising material as sensors in hybrid pixel detectors.

Hybrid pixel X-ray detectors represent the state of the art in imaging detectors on high-end scientific facilities such as synchrotron storage rings and X-ray free electron lasers[1–3]. They comprise a semiconductor sensor electrically connected to pixelated electrodes within an Application Specific Integrated Circuit (ASIC). Unlike indirect conversion detectors, which emit visible light upon X-ray absorption[4,5], hybrid detectors operate via direct conversion. Here, incoming X-ray photons are directly absorbed by the detector's sensor, generating a charge cloud whose total charge carriers are proportional to the incident photon energy. The charge cloud is then transported along the semiconductor's thickness by applying an electric field, producing induced current pulses that are subsequently processed by the ASIC. Many hybrid detectors utilized in light source facilities are built upon Medipix and Timepix ASICs developed by CERN[6], with the latest iteration being the Timepix4 ASIC[7]. Upon proper absorption and charge transport within the sensor, these devices can be employed as pixelated photon counters capable of achieving count-rates over $\sim 10^9$ photons per $mm^2 \times$ s. Consequently, the absorption efficiency and transport properties of the sensor materials play a vital role in determining the overall detection performance of the assembled instrument.

Regarding absorption efficiencies, heavy-element semiconductors are essential for designing high-energy radiation detectors, owing to their superior photo-absorption probabilities due to their large cross-sections. These semiconductors are often referred to as high-Z materials, as they are composed of high atomic number elements, such as CdTe and GaAs[8–10]. In this context, despite lead-based perovskites being extensively explored for solar cells for over a decade[11], their investigation for use in radiation detectors has only recently gained traction[12–14]. While organic-inorganic perovskite compounds, such as $MAPbBr_3$ are mainly regarded for their transport

[1]Brazilian Center for Research in Energy and Materials (CNPEM), Brazilian Synchrotron Light Laboratory (LNLS), Campinas 13083-100, Brazil. [2]State University of Campinas, Institute of Physics "Gleb Wataghin" (IFGW), Campinas 13083-859, Brazil. [3]These authors contributed equally: Jean Marie Polli and Francisco das Chagas Marques. ✉email: raul.campanelli@lnls.br

properties[15], their limited chemical stability hinders their technological suitability for radiation detectors[16]. In contrast, purely inorganic perovskites such as $CsPbBr_3$ offer enhanced chemical stability, rendering them promising alternatives for these applications[13]. Moreover, they have also demonstrated remarkable stability under high energy radiations, even upon a significant amount of dose being deposited onto it[17].

The main features these materials exhibit are high photon absorption probabilities when compared to other semiconductor materials, particularly for incident photon energies above 90 keV. To quantify this characteristic, we compiled their photoelectric cross-sections from NIST via the XCOM database[18]. Photon absorption probabilities were calculated using the Beer-Lambert law, shown in Eq. (1), which computes the intensity I as a function of the sensor thickness L[19].

$$I = I_0 e^{-d\sigma L} \tag{1}$$

where I_0 is the incident intensity, σ is the photo-absorption cross-section, d is the material's density, and $L = 1$ mm. Figure 1 presents the numerical result of Eq. (1), demonstrating the absorption efficiencies for silicon and high-Z sensors (including $CdPbBr_3$), as well as the cross-section values used for this calculation[18].

Among the semiconductors presented in Fig. 1a, $CsPbBr_3$ stands out as the most efficient in detecting X-rays, particularly towards the more energetic end of the spectrum. This is largely attributed to the photo-absorption interactions enabled by the Pb K $1s$ edge, occurring from 88.005 keV onwards. Such characteristics make lead-based perovskites exceptionally interesting for high-energy X-ray detection. Recent studies on inorganic perovskites as radiation sensors have involved experimental prototypes of simple $CsPbBr_3$-based devices under synchrotron radiation, showcasing their potential for handling high incident photon fluxes[20]. These sensors, equipped with guard-rings along their outer edges, demonstrated robust performance, maintaining efficiency at photon fluxes up to 10^{10} photons per $mm^2\times$ s, with slight degradation observed at around 10^{12} photons per $mm^2\times$ s due to the build-up of space charges. Moreover, the authors outlined that greater crystal quality could enhance this performance further.

Pixelated structures, on the other hand, have only recently been realized, by connecting poly-crystalline $CsPbBr_3$ films to Complementary Metal-Oxide Semiconductor (CMOS) readout systems, with pixel pitches around 83 μm[21]. In fact, this work represents a significant advance in perovskite-based detectors, demonstrating the viability of its construction in imaging devices. Nevertheless, the challenge of developing single-crystal imaging sensors, which are presents lower trap-densities, leading to higher collection efficiencies[12], is still

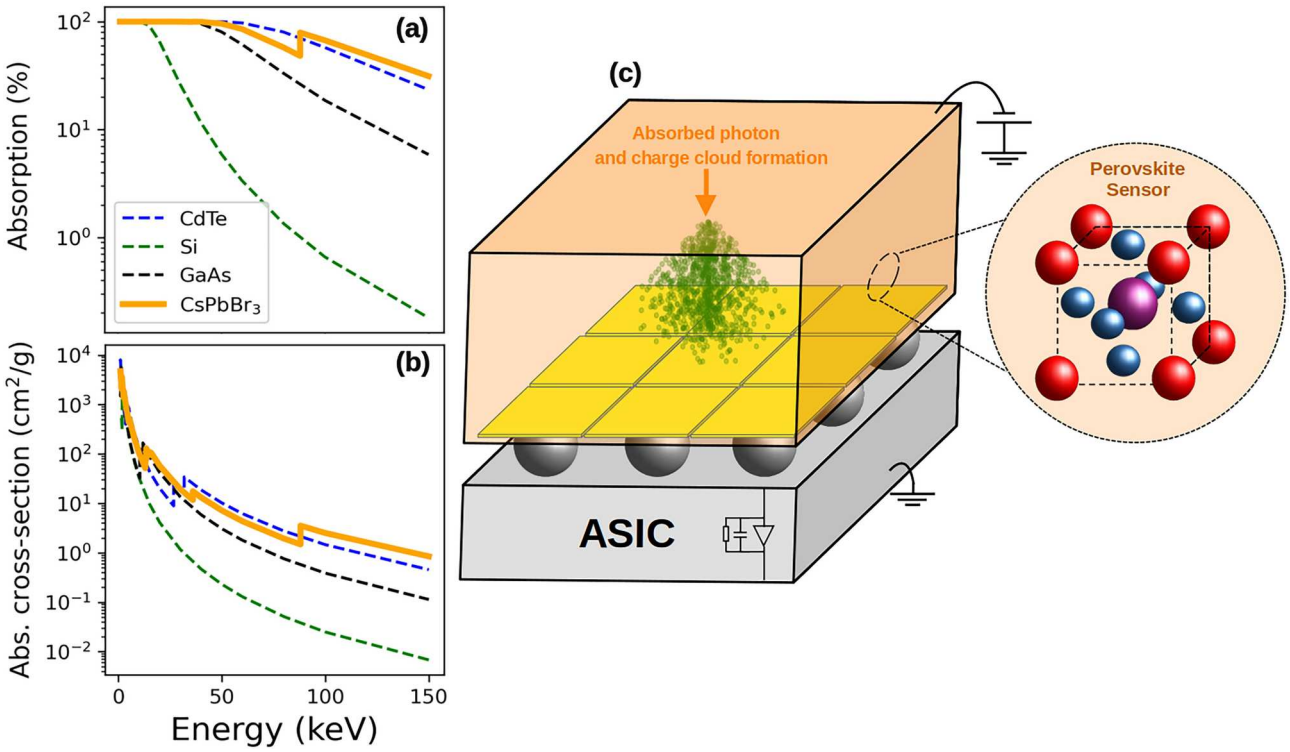

Fig. 1. Perovskite-based hybrid detector. (**a**) Absorption efficiency curve as function of photon energy, calculated using cross-section values in (**b**), and the thickness $L = 1$ mm. (**c**) Schematic depiction of $CsPbBr_3$ sensor on a hybrid detector, demonstrating charge-cloud dynamics. Charge carriers are depicted as green particles dispersed along the sensor's volume. On the right-hand side, the inset presents the Perovskite's crystal structure.

unattended. Furthermore, the integration of such sensors into pixelated photon-counter ASICs, like the 55 μm-pitch Timepix4, requires adaptations to accommodate their smaller pixels and careful consideration of the precise mechanisms governing signal formation in photon-counting detectors. Here, we intend to fulfill this gap by presenting experimental and numerical evaluations of signal formation and detection behavior of these devices.

The signal formation phenomenon is primarily governed by the movement of the photon-generated charge clouds, illustrated in green in Fig. 1, which are driven towards the pixel electrodes through the application of an electric field across the sensor. The field is usually applied via reverse bias polarization, for minimizing leakage currents, and the sensor is typically monolithic, which leads to undesired charge sharing among neighboring pixels. This might be completely avoided upon constructing discrete sensors for every individual pixel. The specific dynamics of each charge carrier along the sensor volume induces a current, *i*, on the pixel electrode, represented in yellow in Fig. 1c. The instantaneous induced current on the electrode is the actual input signal for photon-counting ASICs, and can be calculated via the Schokley–Ramo expression in Eq. (2)[22].

$$i = q\vec{v} \cdot \vec{\epsilon} \tag{2}$$

In Eq. (2), q is the elementary charge of approximately 1.602 $\times 10^{-19}$ C, which scales the dot product between the charge's instant velocity and the weighting field, respectively represented by $\vec{v}$ and $\vec{\epsilon}$. The latter a vector representation of the contribution that a given charge carrier on a point in space exert on the overall signal pulse, and is greatly influenced by the electrode geometry. Conversely, the instant velocity is directly correlated with the carrier mobility, which is significantly affected by crystal quality and fabrication methods. Recent measurements indicate mobility values ranging from 11 to 160 $\mathrm{cm}^2/\mathrm{Vs}$[23–25]. In this context, our work aims to conduct experimental and computational evaluations of the feasibility of $\mathrm{CsPbBr_3}$ as semiconductor sensors in hybrid pixel detectors, focusing on their signal formation behavior. We fabricated our own crystals and measured their carrier mobility, which we subsequently employed to simulate signal formation under various operating conditions. Furthermore, we conducted microelectronic simulations using architectures similar to those found in Timepix4 to assess the ASIC's response to signals generated by $\mathrm{CsPbBr_3}$ sensors.

Results and discussions

To ensure robust data for our assessment, we employed experimental efforts towards single-crystal fabrication and the subsequent characterization of their physical properties. In particular, the mobility measurements are then applied to our computational study comprising signal formation via Shockley-Ramo simulations, as well as pulse shape calculations on Timepix-based ASICs using the LTspice® simulation platform[26]. All data presented in this article are available in the supplementary file Data.zip.

Perovskite crystal growth and characterization

As semiconductor transport properties are significantly influenced by grain boundaries and crystal imperfections, our focus was on synthesizing $\mathrm{CsPbBr_3}$ single-crystals to accurately assess their suitability for constructing hybrid pixel detectors. We adapted a chemical growth method from existing literature sources[23,27], resulting in reproducible sample batches. The growth dynamics of one of our synthesized batches are presented in the Supplementary Video, yielding more than ten crystals per batch with dimensions over the mm^3 range. This is a straight-forward, solution-based growth method, and the overall fabrication results are depicted in Fig. 2.

Our materials present a distinctive orange color and well-formed crystal habits, with sharp edges and straight faces. To confirm the single-crystal profile of our grown materials, we performed Laue diffraction experiments on multiple samples. All of them presented diffraction profiles composed of segregated spots, with no formation of ring-like patterns. This is indicative of single-crystals absent of grain boundaries within the inner crystal volume that could hinder charge carrier propagation. Additionally, upon excitation with a 400 nm ultraviolet laser, we measured their photoluminescence (PL) response. The PL emitted photons' wavelengths are centered at 532 nm, corresponding to a mean energy of 2.31 ± 0.1 eV. This is a well documented property of $\mathrm{CsPbBr_3}$[17,23,25], yielding a characteristic green and bright PL response, as depicted in the inset of Fig. 2b. X-ray diffraction measurements further confirmed the presence of peaks corresponding to the desired $\mathrm{CsPbBr_3}$ structure, revealing a single phase consistent with the Pnma symmetry group[25,28,29]. Through Lebail calculations using the FullProf Suite software[30], we determined the lattice parameters to be 8.25, 11.75, 8.2 Å, similar to previously reported values for $\mathrm{CsPbBr_3}$ perovskites[29]. The calculated structure of the present material is shown in the inset of (c). These results affirm that the presently described material consists of single-crystals with the expected perovskite structure, thus suitable for evaluation as hybrid detector sensors. For this purpose, we analyzed their transport properties by connecting crystals to electrical contacts with different natures. Specifically, we constructed symmetrical Ohmic devices with the C/$\mathrm{CsPbBr_3}$/C configuration, as well as Schottky-based diodes using C/$\mathrm{CsPbBr_3}$/Ag samples. The results obtained from these devices are presented in Fig. 3.

X-ray irradiation with the energy spectrum presented in Supplementary Figure S1 is observed to result in sharp current increases in Fig. 3a,b. During the time-span of these experiments, a noticeable rise in background current is particularly evident for the C/$\mathrm{CsPbBr_3}$/C device. This increase is likely attributable to ionic migrations along the crystal lattice, which are enhanced by the high leakage currents. In contrast, the Schottky sample exhibits much lower leakage current levels, resulting in sharper transitions between dark and X-ray illuminated conditions. Furthermore, the effect of ion migration is less pronounced, leading to a slight decrease in dark current levels and requiring shorter stabilization times compared to the C/$\mathrm{CsPbBr_3}$/C sample. These characteristics make Schottky junctions ideal for constructing perovskite-based hybrid detectors, as minimizing both dark current and stabilization times are crucial considerations in sensor design.

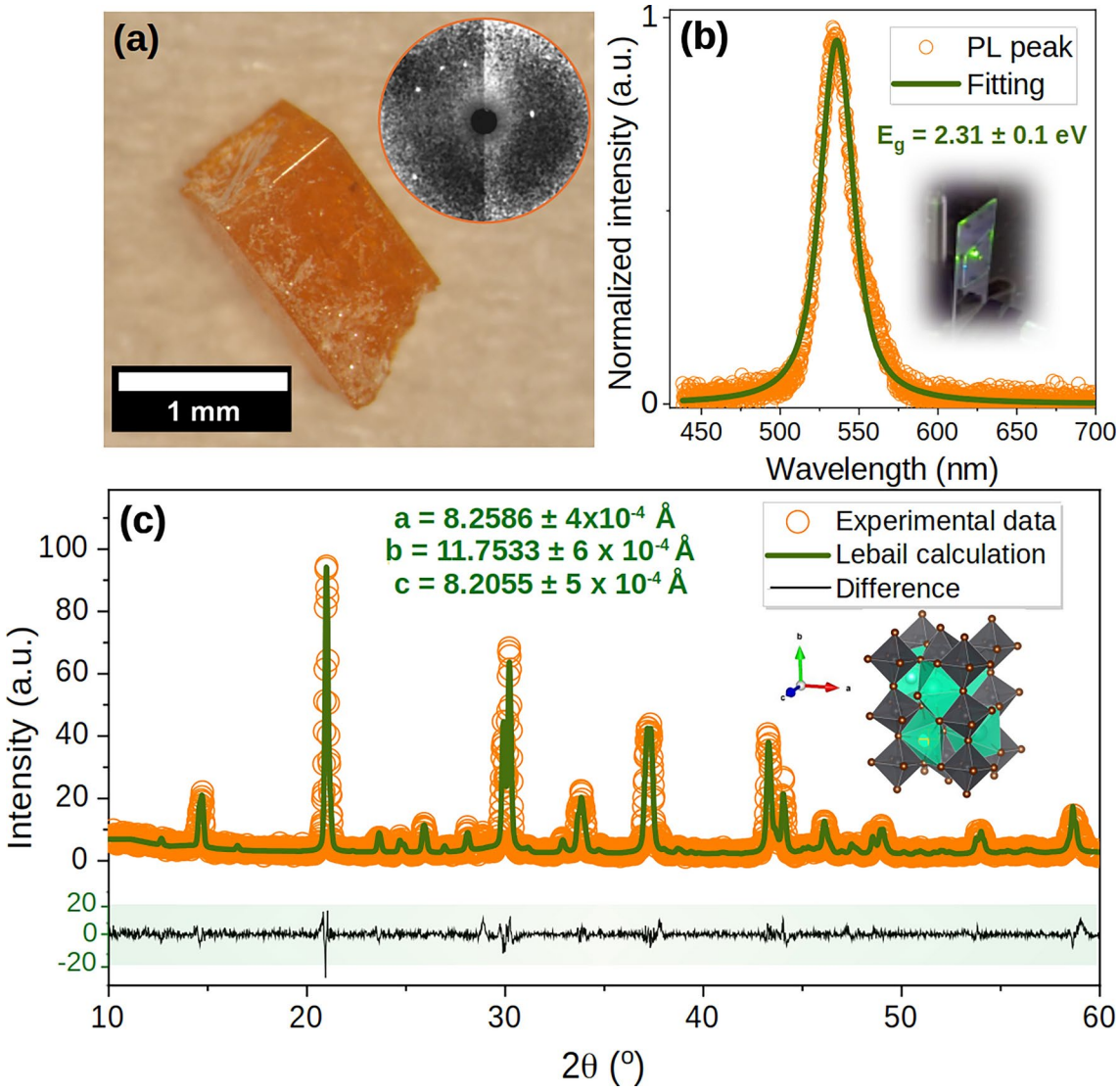

Fig. 2. Characterization of $CsPbBr_3$ crystals. (**a**) Photograph of grown single-crystal. The inset presents a Laue diffraction image. (**b**) Photo-luminescence peak of sample under an excitation source of 400 nm, and photograph of the sample's green light emission. (**c**) X-ray powder diffraction.

To characterize the material's carrier mobility, we employed the Space Charge Limited Current (SCLC) method[23,31], which describes the evolution of three conduction regimes under applied voltage conditions. These regimes can be identified by observing the exponent with which the current density, *J*, evolves with the applied voltages, *V*, accomplished by fitting J^n across the different proportionality regimes. At sufficiently low voltages, the evolution *J* tends to be linear ($n = 1$), followed by a regime of rapid increase with $n > 2$. Finally, the behavior tends to $n = 2$, at which point it becomes possible to apply the Mott-Gurney theorem, described in Eq. (3), to calculate the carrier mobility.

$$\mu = \frac{8JL^3}{9\epsilon_0\epsilon V^2} \tag{3}$$

In Eq. (3), ϵ_0 and ϵ represent the vacuum permittivity and the relative dielectric constant of $CsPbBr_3$ which is approximately 22[23]. This equation is expected to provide an accurate description of mobility for sufficiently large thicknesses (> 50 nm)[32]. It is also important to note that this model assumes the presence of only one carrier species during the measurement period. In our case, since our symmetrical carbon contacts present a work function of around 5 eV, the mobility being measured corresponds to that of holes. By fitting Mott-Gurney's equation to the data within the $n = 2$ regime, we obtained a mobility value of 100.7 ± 0.2 cm^2/Vs, which is compatible with high-quality crystals grown from melt[24], even though our fabrication route consists on a facile solution-based growth. Moreover, the hole mobility values may be further increased by incorporating small

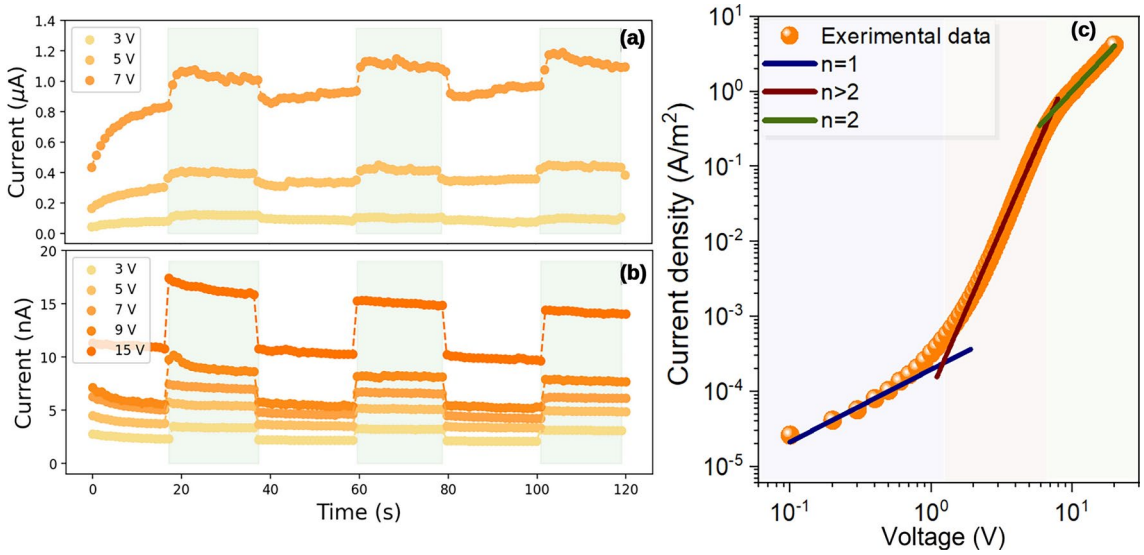

Fig. 3. Transport measurements on $CsPbBr_3$ crystals. (**a**) and (**b**) present the detection behavior under multiple applied voltage conditions, of both C/$CsPbBr_3$/C and C/$CsPbBr_3$/Ag configurations, respectively. Green shaded areas correspond to intervals of X-ray incidence. (**c**) Current density evolution as function of applied voltage. The lines refer to the respective power-law regime of each voltage condition.

iodine doping contents[29]. To investigate $CsPbBr_3$ crystal's performance as X-ray sensors for hybrid detectors, we employed the mobility value obtained in our signal formation simulations.

Signal formation and pulse simulation

The experimentally determined hole mobility value was then employed in the development of Monte Carlo simulations based on the Shockley-Ramo theorem, as described in Eq. (2). The algorithm operates by resolving the spatial propagation step in all three dimensions *x*, *y* and *z* of a given charge carrier during a time interval *dt*. This process is repeated for all generated charge carriers, which, in $CsPbBr_3$, are correlated to the photon energy by an approximate factor of 5[13]. In our simulations, the sensor's thickness was set to 1 mm in the *z* direction. In this initial approximation, the electric field was assumed to be homogeneous and aligned with the *z* direction. For more accurate analyses, a combination of specialized Technology Computer-Aided Design (TCAD) software and advanced programs like Garfield++ can be employed[33]. In our calculations, *z* is perpendicular to the electrode area on the *xy*-plane, and we accounted for drift and diffusion-related spatial displacements, as outlined in Eq. (4).

$$dz_D = \frac{V}{L}\mu\, dt \tag{4}$$

The contribution of diffusion, on the other hand, was implemented in such a way that the direction in which the diffusion propagation step occurs is randomly selected for each time interval *dt*. The average distance traveled by the charge carriers were set as $\sqrt{2D\ dt}$[34], where *D* is the Einstein diffusion coefficient as expressed by Eq. (5), in which k_B is the Boltzmann constant and *T* is the temperature.

$$D = \frac{\mu k_B T}{q} \tag{5}$$

Both holes drift and diffusion are accounted for the simulation of individual charge trajectories, which are then utilized for calculating signal formation from Eq. (2). Consequently, the overall signal amplitude emerges from the cumulative induced current produced by all charge trajectories, as exemplified in Fig. 4a. The numerical parameters used for our calculations, as well as the method for determining $\bar{\epsilon}$ are detailed in the Methods section. As a result, we have simulated a series of induced current pulses on Timepix4 input electrodes, as depicted in Fig. 4.

The direct consequence of high incident energies is the generation of densely populated charge clouds. Additionally, Fig. 4a illustrates its effect on signal formation for 900 V biased $CsPbBr_3$ sensors, showing a clear increase in pulse amplitude with higher energies. Conversely, the variation in incident energy does not significantly affect the overall pulse width (Fig. 4b). This is evident because the variations in the time intervals required to integrate 90 % of the induced charges fall within one standard deviation for a given bias value. Concerning the influence of applied voltages, pulse widths can be substantially reduced for higher bias voltages.

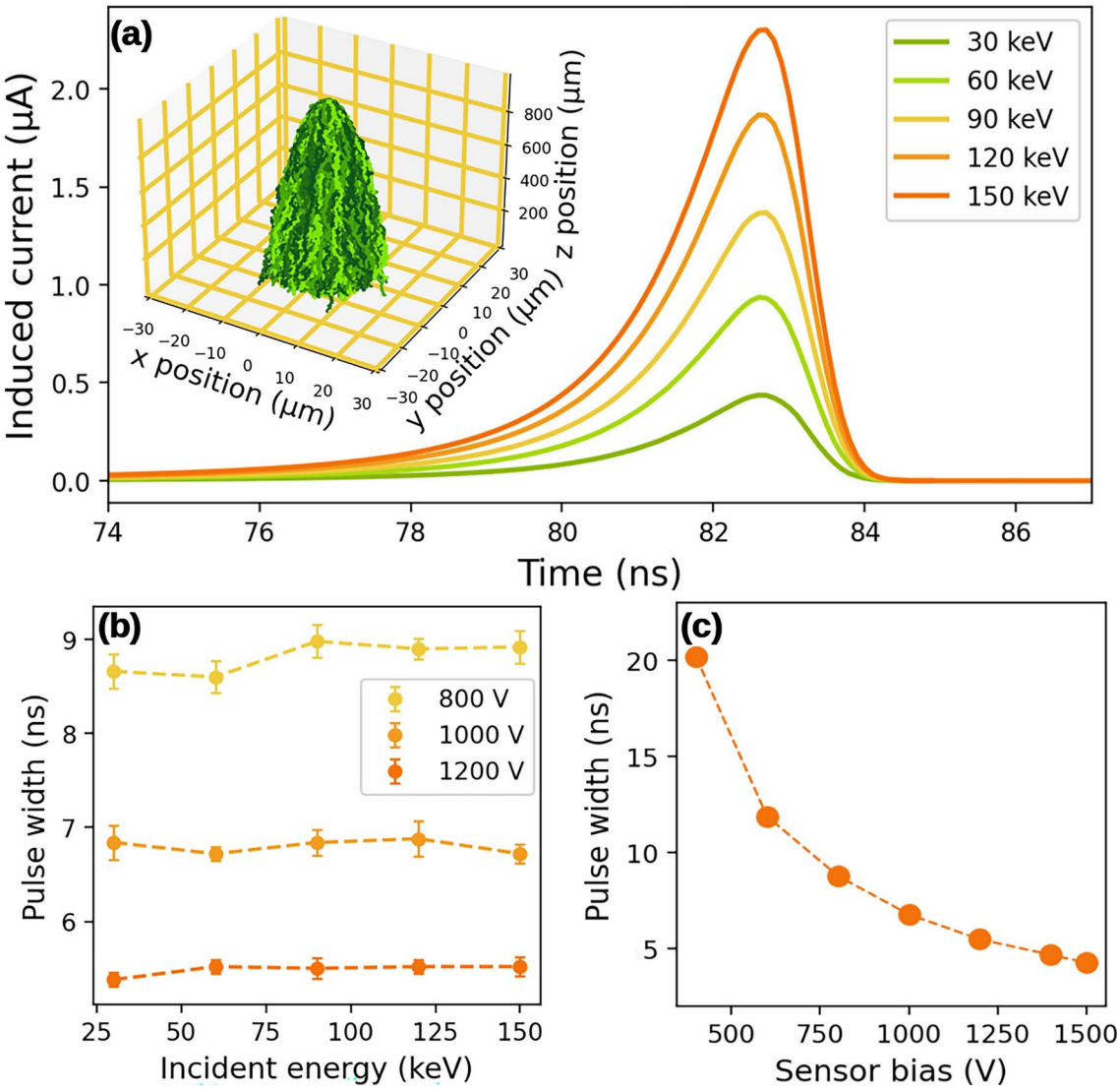

Fig. 4. Simulation of signal formation in a 1 mm-thick $CsPbBr_3$ sensor on a 44 μm sided square electrode via Shockey–Ramo calculations. (**a**) Induced current originated by different incident photon energies, where the inset shows the simulation of charge trajectories. (**b**) and (**c**) show the time-interval required for integrating 90 % of the induced charges as function of incident energy and applied voltages, respectively. The first one was calculated for applied bias values of 800, 1000, and 1200 V, while the latter was performed for 90 keV photons.

Indeed, applied biases of approximately 800 V yield pulse widths around the characteristic rise-time intervals of Timepix4 of 10 ns[7]. This suggests that lower applied biases may lead to ballistic deficits[35], a chromatic aberration deteriorating signal integrity due to incomplete charge integration on the ASIC. To gain deeper insights into the interplay between the generated pulses on $CsPbBr_3$ sensors, we extended our pulse simulations to serve as input data for LTspice® simulation routines estimating an approximate behavior of Timepix4.

A fundamental component on Timepix4 is the Krummenacher pre-amplifier[36]. It comprises a Charge-Sensitive Amplifier with a Krummenacher feedback discharge path and a leakage compensation circuit. As the feedback drains the gain capacitor charge with constant current through the baseline level, the Krummenacher amplifier discharge duration is directly proportional to the incident photon energy. Thus, by establishing a constant voltage threshold, the incident photon energy can be ascertained by measuring the duration for which the Krummenacher pulse remains above the threshold level. This measurement technique is referred to as time-over-threshold (ToT)[37]. For analysing this behavior, we developed a simulation model on LTspice® approximating the reported conditions for Timepix4 ASICs, resulting in an approximate 10 ns output rise time. This simulator was employed to estimate the expected output response of a Krummenacher amplifier generated by the input pulses derived from our Shockley-Ramo calculations, such as the ones depicted in Fig. 4. The Krummenacher output results are shown in Fig. 5.

Notably, the increase in amplitude previously described in Fig. 4a reaches a saturation limit upon Krummenacher amplification, as depicted in Fig. 5a. However, this energy saturation does not apply to the ToT measurements, which remain fairly linear across the probed spectrum, as shown in (b). Therefore, this well-

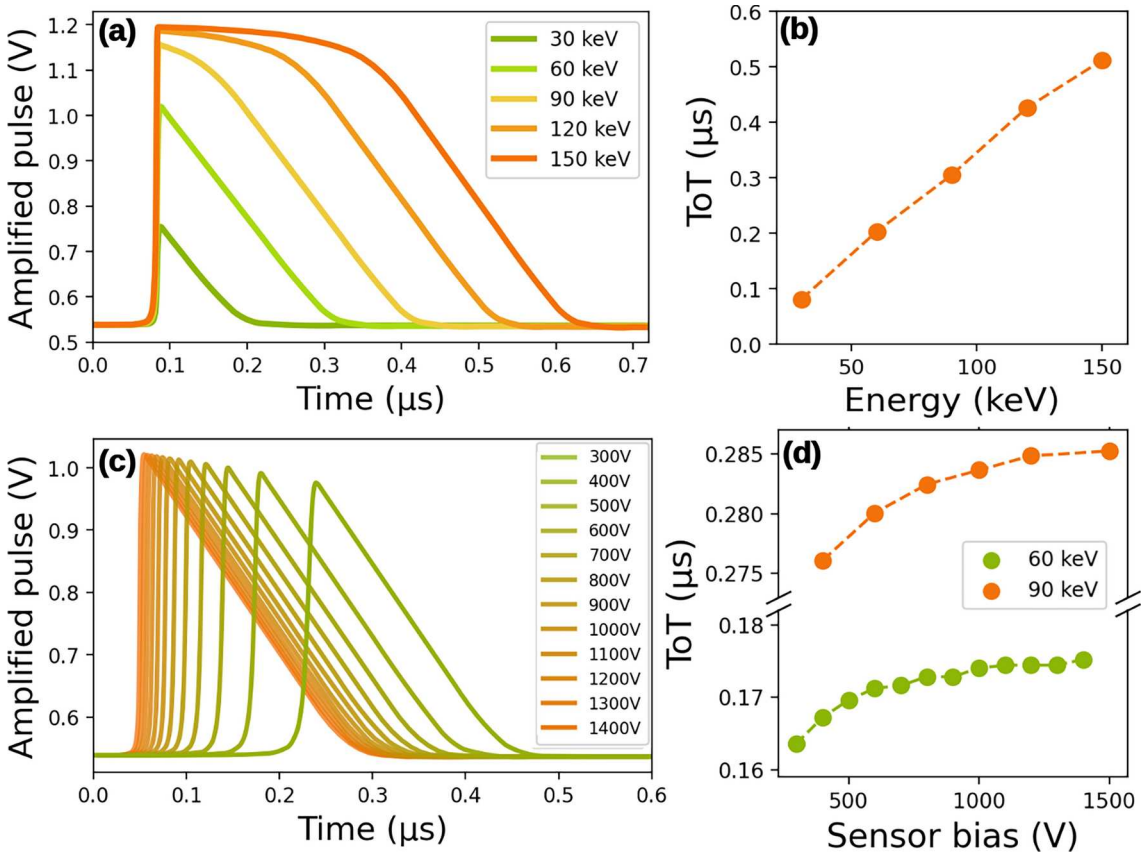

Fig. 5. Krumenacher output simulations, with inputs originated from induced currents on a 44 μm sided square electrode attached to a 1 mm-thick $CsPbBr_3$ sensor. (**a**) Pulse shapes for photon energies ranging from 30 to 150 keV. (**b**) ToT values for pulses in (**a**). (**c**) Outputs for 60 keV photons for multiple sensor bias values. (**d**) ToT values as a function of the sensor bias for 60 nad 90 keV.

known characteristic of Krummenacher amplifiers is preserved for our simulated $CsPbBr_3$ sensors under the aforementioned operating conditions. Regarding variations in bias voltages, not only do they exert a notable effect in the instant in which the amplified signal start to rise, but it also may lead to a loss of detected energy due to the ballistic deficit under low bias conditions. The simulated outputs for 60 keV incident photons into $CsPbBr_3$ under multiple bias values are shown in (c), wherein the effect of reduced bias is visible as a delay in the output pulse, as well as a slight amplitude deterioration. On the other hand, ToT calculations exhibit notably diminished readings below 900 V. For bias values above 1000 V, a fairly stable ToT reading is obtained for both 60 and 90 keV (Fig. 5d,e), indicating that the ballistic deficit is no longer an issue within this regime. Hence, our findings reinforce the importance of establishing appropriate bias conditions to ensure the effective utilization of $CsPbBr_3$ as sensors in hybrid detectors. Additionally, we demonstrate that electric fields around 1 kV/mm, which have already been applied to $CsPbBr_3$ and other high-Z materials[20,38], provide sufficient conditions for optimal operation. Fortunately, even though GaAs and CdTe demand less intense applied biases as they present higher carrier mobility values[10,39], the requirements for $CsPbBr_3$ fall well within the typical operation capabilities of hardware design. Thinner sensors could also be a viable option when specific requirements for lower operating voltages need to be met. However, this would result in decreased absorption efficiency, as described in Eq. (1). Moreover, the increase of mobility values provided by iodine doping may further reduce the required applied biases[29]. In addition to actual device fabrication, future work will also address other aspects of the application of this material, such as the role of K-alpha emissions from all three elements, which are summarized in the Supplementary Table.

Conclusions

This study offers a comprehensive analysis of the X-ray detection behavior of $CsPbBr_3$ crystals, establishing optimal operational conditions for detector design. We successfully synthesised single-crystals via a straightforward chemical route, and performed several characterization experiments, including X-ray crystallography and photo current measurements, which exhibited similar results to those found on the literature. Moreover, our results enabled the determination of their transport properties such as carrier mobility, which was found to be equal to $100.7 \pm 0.2\ cm^2/Vs$. This value served as a crucial parameter for simulating X-ray detection behavior, revealing a robust correlation between applied bias and induced current pulse width. Using a 44 μm-sided square electrode, our simulations showed an average interval of 6.9 ns for integrating 90 % of generated charges

under 1000 V/mm. Through LTspice® simulations using a Krummenacher-based pre-amplifier model, we assessed $CsPbBr_3$ performance as sensors in hybrid detectors under various operational conditions. Our results demonstrate that the signals generated by high-energy photon hits are effectively integrated with bias voltages around 1000 V. Future efforts on perovskite-based hybrid detectors should focus on assembly strategies, and experimental performance metrics, including as spatial and energy resolutions. Spectral response upon X-ray excitation, the effects exerted by fluorescence emissions, as well as novel assembly concepts (e.g. discrete sensors for each individual pixel) are also on our road-map.

Methods

Crystal growth

Our synthesis procedure follows the methodology outlined by Saidamov et al.[23]. It begins by diluting 1:2 molar ratios of $CsBr : PbBr_2$ in Dimethyl sulfoxide (DMSO). Specifically, we mixed 0.3192 g of CsBr, 1.101 g of $PbBr_2$ in 1.5 mL DMSO, all purchased from Sigma Aldrich, inside a glass vial. After complete dissolution of the powders, the vial containing the mixture was placed in a glass beaker filled with glycerin. The bath was then heated to 60° C using a hot plate with temperature feedback control.. The temperature was then slowly increased at a rate of $10\,^\circ$C/h, up to $100\,^\circ$C. At this temperature, some undesired precipitates began to form, which could be easily separated from the liquid using a 45 μm filter. The clean liquid is then transferred to another vial pre-heated to 100°C, where the growth procedure continued by maintaining it at a constant temperature overnight. The Supplementary Video presents a time-lapse video recording of the final stage of the synthesis method, demonstrating the nucleation and growth of $CsPbBr_3$ single-crystals over approximately five hours.

Experimental characterizations

To correctly identify the $CsPbBr_3$ crystal structure, we conducted powder X-ray diffraction experiments by grinding the grown crystals and analyzing them using a Brucker diffractometer system equipped with a Cu Kα source. The obtained results were analyzed with the FullProf Suite software[30], enabling the determination of lattice parameters of the grown structure. The Laue pattern was obtained with a Siemens X-Ray tube combined with a CCD camera, and the PL measurements were performed by directing 400 nm light into the crystals, and recording the results with a UV-Vis spectrometer.

For electrical characterizations, Ohmic contacts were fabricated by attaching carbon-based tape to opposite sides of a 602 μm-thick crystal. For the Schottky samples, one side was coated with Ag-rich epoxy resin, while the other side was also attached to carbon-based tape, using a 630 μm thick crystal. These experiments were conducted within a grounded metallic enclosure shielded from visible light. To expose the crystals to X-rays, we utilized a Mini-X generator from Amptek operating under 40 kV and 100 μA settings, generating the spectrum shown in Supplementary Figure S1. Current measurements were acquired using a Keithley 6517A electrometer, controlled by our automation implemented as a Python3 script, from which we also applied bias voltages onto the crystals. This allowed the measurement of our crystals' carrier mobility, which was then used for computational characterization for assessing the suitability of $CsPbBr_3$ as X-ray sensor material in hybrid pixel detectors.

Computational characterizations

Our signal formation simulation is implemented as a Python3 script designed to solve multiple carrier trajectories based on drift and diffusion mechanisms, while calculating the instantaneous induced current as presented in Eq. (2). In the present calculations, we utilized time steps of 5×10^{-11} s, and the simulated sensor thickness was set to 1 mm. Given that photoelectric absorption results in all generated charges being centered around a single point in space, we assumed the initial positions of all carriers to be at this point. This approximation is valid, as the photoelectric effect dominates the photon interaction phenomena across the entire energy spectrum we probed, as shown in our Supplementary Text in Fig. S3. Although varying energies should result in different distributions of initial positions, for the purpose of pulse comparison under the equivalent conditions, all charge carriers were initiated from a single point within the simulated sensor volume, located at $x = y = 0$ and $z = 700\ \mu m$. While this condition may not fully represent all possible initial depths, we anticipate that most signal formation occurs near the collection electrode, where $\bar{\epsilon}$ is more intense, commonly referred to as the "small pixel effect"[40]. For a more realistic calculation, the absorption depths could be varied across multiple pulses to reflect the absorption depth distributions associated with each energy. In our coordinate system, the point $x = y = z = 0$ corresponds to the center of the squared electrode of lattice ($a = 44\mu$m) which is equivalent to the geometries of some versions of the Medipix collaboration ASICs[22,41]. The calculation of $\bar{\epsilon}$ was performed for each time-step using Eq. (6)[40].

$$\vec{\epsilon} = \nabla\Omega = \frac{1}{2\pi}\nabla\left\{ tan^{-1}\left[\frac{(a-x)(a-y)}{z\sqrt{(a-x)^2+(a-y)^2+z^2}}\right] + tan^{-1}\left[\frac{(a-x)(a+y)}{z\sqrt{(a-x)^2+(a+y)^2+z^2}}\right] + tan^{-1}\left[\frac{(a+x)(a-y)}{z\sqrt{(a+x)^2+(a-y)^2+z^2}}\right] + tan^{-1}\left[\frac{(a+x)(a+y)}{z\sqrt{(a+x)^2+(a+y)^2+z^2}}\right]\right\} \tag{6}$$

In the equation above, Ω represents the weighting potential, from which we are able to determine $\bar{\epsilon}$ along every point within the charge-carriers' trajectories. The distribution of Ω for a semi-continuous three-dimensional space containing our simulated electrode is depicted in Supplementary Figure S2. The simulated pulses were then utilized as input sources in the LTspice® simulation platform, configured to model the behavior of a Krummenacher pre-amplifier. To achieve comparable rise-times and pulse duration to those observed on Timepix4, adjustments were made to the gain capacitor and leakage current compensations.

Data availability

All data generated or analysed during this study are included in this published article.

Received: 6 August 2024; Accepted: 25 September 2024
Published online: 09 November 2024

References

1. Förster, A., Brandstetter, S. & Schulze-Briese, C. Transforming x-ray detection with hybrid photon counting detectors. *Phil. Trans. R. Soc. A* **377**, 20180241 (2019).
2. Campanelli, R. et al. Large area hybrid detectors based on Medipix3RX: Commissioning and characterization at Sirius beamlines. *J. Instrum.* **18**, C02008 (2023).
3. Sztuk-Dambietz, J. et al. Operational experience with adaptive gain integrating pixel detectors at European XFEL. *Front. Phys.* **11**, 1329378 (2024).
4. Mykhaylyk, V. et al. Bright and fast scintillations of an inorganic halide perovskite CsPbBr3 crystal at cryogenic temperatures. *Sci. Rep.* **10**, 8601 (2020).
5. Datta, A., Fiala, J. & Motakef, S. 2d perovskite-based high spatial resolution x-ray detectors. *Sci. Rep.* **11**, 22897 (2021).
6. Ballabriga, R., Campbell, M. & Llopart, X. Asic developments for radiation imaging applications: The medipix and timepix family. *Nucl. Instrum. Methods Phys. Res. Sect. A* **878**, 10–23 (2018).
7. Llopart, X. et al. Timepix4, a large area pixel detector readout chip which can be tiled on 4 sides providing sub-200 ps timestamp binning. *J. Instrum.* **17**, C01044 (2022).
8. Lee, S. et al. Direct thermal growth of large scale cl-doped CdTe film for low voltage high resolution x-ray image sensor. *Sci. Rep.* **8**, 14810 (2018).
9. Zat'ko, B. et al. Imaging performance of a Timepix detector based on semi-insulating GaAs. *J. Instrum.* **13**, C01034 (2018).
10. Vicini, V. et al. Optimization of quasi-hemispherical CdZnTe detectors by means of first principles simulation. *Sci. Rep.* **13**, 3212 (2023).
11. Stranks, S. D. & Snaith, H. J. Metal-halide perovskites for photovoltaic and light-emitting devices. *Nat. Nanotechnol.* **10**, 391–402 (2015).
12. Wu, H., Ge, Y., Niu, G. & Tang, J. Metal halide perovskites for x-ray detection and imaging. *Matter* **4**, 144–163 (2021).
13. He, Y. et al. High spectral resolution of gamma-rays at room temperature by perovskite cspbbr3 single crystals. *Nat. Commun.* **9**, 1609 (2018).
14. Wei, H. & Huang, J. Halide lead perovskites for ionizing radiation detection. *Nat. Commun.* **10**, 1066 (2019).
15. Dong, Q. et al. Electron-hole diffusion lengths> 175 μm in solution-grown ch3nh3pbi3 single crystals. *Science* **347**, 967–970 (2015).
16. Yuan, Y. & Huang, J. Ion migration in organometal trihalide perovskite and its impact on photovoltaic efficiency and stability. *Acc. Chem. Res.* **49**, 286–293 (2016).
17. Gao, L., Sun, J.-L., Li, Q. & Yan, Q. γ-ray radiation hardness of cspbbr3 single crystals and single-carrier devices. *ACS Appl. Mater. Interfaces* **14**, 37904–37915 (2022).
18. Berger, M. et al. *Nist standard reference database 8 (XGAM)* (NIST, PML, Radiation Physics Division, 2010).
19. Lowe, B. G. & Sareen, R. A. *Semiconductor X-ray Detectors* (CRC Press, Boca Raton, 2014).
20. Pan, L. et al. Study of perovskite CsPbBr 3 detector polarization and its mitigation with ultrahigh x-ray flux. *J. Appl. Phys.* **133**, 194502 (2023).
21. Liu, Y. et al. Dynamic x-ray imaging with screen-printed perovskite CMOS array. *Nat. Commun.* **15**, 1588 (2024).
22. Manach, E. & Gal, O. Experimental and simulation results of gamma imaging with hybrid pixel detectors. *Nucl. Instrum. Methods Phys. Res., Sect. A* **531**, 38–51 (2004).
23. Saidaminov, M. I. et al. Inorganic lead halide perovskite single crystals: Phase-selective low-temperature growth, carrier transport properties, and self-powered photodetection. *Adv. Opt. Mater.* **5**, 1600704 (2017).
24. Zhang, P. et al. Enhancing carrier transport properties of melt-grown cspbbr3 single crystals by eliminating inclusions. *Crystal Growth Des.* **20**, 2424–2431 (2020).
25. Peng, J. et al. Crystallization of cspbbr3 single crystals in water for x-ray detection. *Nat. Commun.* **12**, 1531 (2021).
26. Asadi, F. *Essential Circuit Analysis Using LTspice®* (Springer Nature, Berlin, 2022).
27. Li, J. et al. Non-traditional positively-biased narrow-band perovskite single-crystal photodetectors enabled by interfacial engineering. *Adv. Opt. Mater.* **10**, 2102225 (2022).
28. Møller, C. K. Crystal structure and photoconductivity of Caesium Plumbohalides. *Nature* **182**, 1436–1436 (1958).
29. Zhang, P. et al. Ultrasensitive and robust 120 keV hard x-ray imaging detector based on mixed-halide perovskite cCsPbBr3 -nIn single crystals. *Adv. Mater.* **34**, 2106562 (2022).
30. Rodríguez-Carvajal, J. Recent advances in magnetic structure determination by neutron powder diffraction. *Phys. B* **192**, 55–69 (1993).
31. Haruta, Y., Ikenoue, T., Miyake, M. & Hirato, T. Fabrication of (101)-oriented cspbbr3 thick films with high carrier mobility using a mist deposition method. *Appl. Phys. Express* **12**, 085505 (2019).
32. Röhr, J. A., Moia, D., Haque, S. A., Kirchartz, T. & Nelson, J. Exploring the validity and limitations of the Mott–Gurney law for charge-carrier mobility determination of semiconducting thin-films. *J. Phys.: Condens. Matter* **30**, 105901 (2018).
33. Schindler, H. *Microscopic simulation of particle detectors*. Ph.D. thesis, CERN (2012).
34. Novikov, A., Kuzmin, D. & Ahmadi, O. Random walk methods for Monte Carlo simulations of Brownian diffusion on a sphere. *Appl. Math. Comput.* **364**, 124670 (2020).
35. Ballabriga, R. et al. Review of hybrid pixel detector readout ASICs for spectroscopic x-ray imaging. *J. Instrum.* **11**, P01007 (2016).
36. Krummenacher, F. Pixel detectors with local intelligence: An IC designer point of view. *Nucl. Instrum. Methods Phys. Res. Sect. A* **305**, 527–532 (1991).
37. Becker, R. et al. Signal processing in the front-end electronics of BaBar vertex detector. *Nucl. Instrum. Methods Phys. Res. Sect. A* **377**, 459–464 (1996).
38. Bettelli, M. et al. High performance platinum contacts on high-flux CdZnTe detectors. *Sci. Rep.* **13**, 17963 (2023).
39. Ballabriga, R. et al. Photon counting detectors for x-ray imaging with emphasis on CT. *IEEE Trans. Radiat. Plasma Med. Sci.* **5**, 422–440 (2020).
40. Eskin, J. D. *Semiconductor gamma-ray detectors for nuclear medicine*. Ph.D. thesis, The University of Arizona (1997).
41. Ballabriga, R. *The Design and Implementation in* $0.13\mu m$ *CMOS of an Algorithm Permitting Spectroscopic Imaging with High Spatial Resolution for Hybrid Pixel Detectors*. Ph.D. thesis, CERN (2009).

Acknowledgements
The authors would like to acknowledge the tecnical support of Simone Bau Betim and the staff of the Chemistry Laboratory of LNLS. We are also thankful for the support of Danusa do Carmo e Rogério M. Grossi for their assistence in material characterization. Finally, we acknowledge the financial support provided by the Brazilian Ministry of Science, Technology and Innovation.

Author contributions
R.B. Campanelli synthesised samples, performed crystal characterization, conducted signal formation simulations, treated data and wrote the present manuscript. G.S. Gomes performed LTspice® simulations. M.M. Donatti built the automation platform for transport measurements, contributed with text writing, assisted in pulse calculations and Krummenacher simulations. L.S. Perissinotto built and operated the hardware systems for electrical measurements. A.D. Pereira, E.B. Antonio, P.L. Vincoletto configured and operated the X-ray experimental setups. M.G. Fernandes contributed with text writing and discussions. L.S. Araujo assisted in $CsPbBr_3$ crystal synthesis, contributed to literature revision and text writing. J.M. Polli and F.C. Marques conceived the project, gathered resources and contributed with text writing and discussions.

Declarations

Competing interests
The authors declare no competing interests.

Additional information
Supplementary Information The online version contains supplementary material available at https://doi.org/10.1038/s41598-024-74384-7.

Correspondence and requests for materials should be addressed to R.B.C.

Reprints and permissions information is available at www.nature.com/reprints.

Publisher's note Springer Nature remains neutral with regard to jurisdictional claims in published maps and institutional affiliations.